remote sensing

MDPI

Article

Global Satellite Retrievals of the Near-Surface Atmospheric Vapor Pressure Deficit from AMSR-E and AMSR2

Jinyang Du [1,*], John S. Kimball [1], Rolf H. Reichle [2], Lucas A. Jones [1], Jennifer D. Watts [1,3] and Youngwook Kim [1]

1 Numerical Terradynamic Simulation Group, W.A. Franke College of Forestry and Conservation, The University of Montana, Missoula, MT 59812, USA; johnk@ntsg.umt.edu (J.S.K.); lucas.jones1@mso.umt.edu (L.A.J.); jwatts@whrc.org (J.D.W.); youngwook.kim@ntsg.umt.edu (Y.K.)
2 NASA Goddard Space Flight Center, Greenbelt, MD 20771, USA; rolf.reichle@nasa.gov
3 Woods Hole Research Center, Falmouth, MA 02540, USA
* Correspondence: jinyang.du@ntsg.umt.edu; Tel.: +1-406-243-5522

Received: 19 June 2018; Accepted: 24 July 2018; Published: 25 July 2018

Abstract: Near-surface atmospheric Vapor Pressure Deficit (VPD) is a key environmental variable affecting vegetation water stress, evapotranspiration, and atmospheric moisture demand. Although VPD is readily derived from in situ standard weather station measurements, more spatially continuous global observations for regional monitoring of VPD are lacking. Here, we document a new method to estimate daily (both a.m. and p.m.) global land surface VPD at a 25-km resolution using a satellite passive microwave remotely sensed Land Parameter Data Record (LPDR) derived from the Advanced Microwave Scanning Radiometer (AMSR) sensors. The AMSR-derived VPD record shows strong correspondence (correlation coefficient $\geq$ 0.80, p-value < 0.001) and overall good performance (0.48 kPa $\leq$ Root Mean Square Error $\leq$ 0.69 kPa) against independent VPD observations from the Modern-Era Retrospective analysis for Research and Applications, Version 2 (MERRA-2) data. The estimated AMSR VPD retrieval uncertainties vary with land cover type, satellite observation time, and underlying LPDR data quality. These results provide new satellite capabilities for global mapping and monitoring of land surface VPD dynamics from ongoing AMSR2 operations. Overall good accuracy and similar observations from both AMSR2 and AMSR-E allow for the development of climate data records documenting recent (from 2002) VPD trends and potential impacts on vegetation, land surface evaporation, and energy budgets.

Keywords: vapor pressure deficit; humidity; AMSR-E/2; MERRA-2; passive microwave remote sensing

1. Introduction

Vapor Pressure Deficit (VPD), defined as the difference between saturated and actual atmospheric vapor pressures at a particular temperature [1], is an important environmental variable that quantifies the atmospheric moisture demand influencing evapotranspiration, latent heat exchange, and the surface energy budget [2,3]. VPD also influences vegetation water stress, canopy photosynthesis, and global carbon and climate feedbacks through vegetation canopy stomatal regulation of both water vapor and carbon dioxide (CO_2) exchange with the atmosphere [2,4,5]. Near-surface VPD defines the atmospheric moisture deficit in the foundational Penman-Monteith equation for estimating latent energy exchange and evapotranspiration [6,7], and also provides a critical environmental input for operational satellite-based methods for predicting global evapotranspiration and ecosystem productivity [8–10]. Variations in VPD have been found to influence global crop yields [11]

and vegetation phenology [12], whereas excessive VPD levels have been linked to drought stress in forests and grasslands [13,14]. Knowledge of global VPD dynamics is therefore required to characterize carbon-water coupling in ecosystems, analyze drought and climate variability and impacts, and improve understanding of terrestrial water, carbon, energy budgets, and linkages.

Global VPD distribution can be obtained from operational atmospheric data assimilation systems targeted at numerical weather prediction [15]. Multi-decadal records from such systems are readily available from reanalysis data products, such as the Modern-Era Retrospective Analysis for Research and Applications (MERRA) [16,17], the European Centre for Medium-Range Weather Forecasts (ECMWF) ERA-Interim product [18], and the National Centers for Environmental Prediction-National Center for Atmospheric Research (NCEP-NCAR) reanalysis [19–21].

Alternatively, direct measurements of near-surface air temperature and humidity from a variety of space-borne sensors also enable independent global observation-based VPD retrievals [22–24]. Most remote sensing approaches rely on optical-infrared (optical-IR) sensors due to their sensitivity to temperature and atmospheric water vapor. For example, simple linear models were used to predict VPD from Moderate Resolution Imaging Spectroradiometer (MODIS) land surface temperature observations, with resulting VPD estimation uncertainties ranging from 0.32 to 0.38 kPa (Root Mean Squared Error; RMSE) for VPD below 2.5 kPa [23]. In a separate study, both MODIS humidity and temperature observations were used to estimate VPD over China, resulting in associated RMSE uncertainties ranging from 0.32 to 0.37 kPa [24]. Similar VPD estimates derived using the National Oceanic and Atmospheric Administration (NOAA) Advanced Very High Resolution Radiometer (AVHRR) resulted in RMSE levels ranging from 0.17 to 1.09 kPa, depending on the region and temporal aggregation examined [22,25,26]. Global VPD products can be derived from lower troposphere temperature and humidity estimates from the National Aeronautics and Space Administration (NASA) Atmospheric Infrared Sounder (AIRS). The version 006 AIRS land product provides a continuous global record of atmospheric temperature and humidity profiles extending from 2002 to present (2018), and has been used for studying land-atmosphere feedbacks at the global scale [27,28]. AIRS has a similar local sampling time as the Advanced Microwave Scanning Radiometer (AMSR) sensors but has coarser (~50 km) spatial resolution retrievals [27].

Compared with global reanalysis data, which have a relatively coarse spatial resolution typically of about 50 km, much finer-scale VPD estimates can be derived from satellite optical-IR remote sensing including MODIS 1-km resolution retrievals [24]. However, global VPD mapping at high temporal resolutions is challenging for space-borne optical-IR sensors, which are constrained by non-optimal atmospheric conditions such as persistent cloud cover and atmospheric aerosols.

Complementary to global reanalysis and optical-IR remote sensing, satellite passive microwave radiometers are sensitive to air temperature and atmospheric water vapor, enabling global estimation of VPD with one- to three-day fidelity and approximately 25 km spatial resolution [29–31]. In particular, multi-frequency brightness temperature (T_b) retrievals from the JAXA Advanced Microwave Scanning Radiometer 2 (AMSR2) and NASA Advanced Microwave Scanning Radiometer for EOS (AMSR-E) sensors have been used for estimating near-surface (two-meter height) air temperature and total column atmospheric water vapor, while mitigating potential contaminating effects from surface water inundation, vegetation biomass, and soil moisture [30,32]. VPD was estimated over the pan-Arctic domain using AMSR-E-derived surface air temperatures [9,29]; the results showed favorable accuracy (0.3–0.4 kPa RMSE) in relation to VPD measurements from regional tower sites [9].

A major assumption of these studies is that the dew-point temperature (T_d) can be approximated by daily minimum air temperature, which is generally valid at high latitudes but can lead to large errors in warmer, drier climate conditions [9,29,33]. A more rigorous estimate of dew-point temperature or surface air humidity is needed for deriving VPD globally. In this study, we developed a new satellite remote sensing approach to estimate the near-surface (~2 m height) VPD using an available Land Parameter Data Record (LPDR) derived from calibrated AMSR-E and AMSR2 T_b observations.

The datasets, methods, and results from this study are described in Sections 2–4, and a discussion of algorithm performance and the study conclusions are presented in Sections 5 and 6, respectively.

2. Datasets

Three major datasets were used for generating and validating the satellite remote sensing derived global VPD records, including: (1) the Version 2.0 UMT Land Parameter Data Record (LPDR) produced from calibrated AMSR-E and AMSR2 (hereafter denoted as AMSR) T_b observations [32]; (2) Integrated Surface Global Hourly (ISH) meteorological data provided by the NOAA National Climatic Data Center (NCDC; https://catalog.data.gov/dataset/integrated-surface-global-hourly-data-f6180); and (3) MERRA, Version 2 (MERRA-2) 2-dimensional atmospheric single-level diagnostics Version 5.12.4 (tavg1_2d_slv_Nx) global reanalysis [34] (https://gmao.gsfc.nasa.gov/reanalysis/MERRA-2/). The 2010 and 2013 annual records, representing respective AMSR-E and AMSR2 observation periods, were extracted from the three datasets for quantitative analysis of the AMSR-derived VPD retrievals in this study. In addition, the National Snow and Ice Data Center (NSIDC) 25-km EASE-Grid elevation dataset [35] re-sampled from a native 1-km resolution global digital elevation map (http://www.ngdc.noaa.gov/mgg/topo/globe.html) was used to account for terrain effects on the AMSR-based VPD estimates.

2.1. AMSR LPDR

The space-borne radiometers AMSR-E (operational from June 2002 to October 2011) and AMSR2 (operational from May 2012 to present) provide twice daily (1:30 p.m. and 1:30 a.m. local time) T_b observations at multiple frequencies (C- to W-band) worldwide since 2002 [36,37]. The AMSR LPDR algorithms were developed for global mapping of multiple synergistic land parameters, including daily maximum and minimum surface air temperature at approximate 2-m screen height (T_{mx} and T_{mn}), total column atmospheric precipitable water vapor (*PWV*), vegetation optical depth (*VOD*), surface fractional open water cover (*fw*), and volumetric soil moisture (*vsm*). The satellite sensor footprint and sensitivity of the T_b observations to land surface conditions vary with microwave frequency and polarization, and are determined by the emissivity and physical temperature of the satellite observed media. The LPDR algorithms exploit the multi-frequency and vertically- and horizontally-polarized (V-pol, H-pol) T_b observations available from the AMSR sensors for near simultaneous iterative estimation of multiple land parameters, with minimal requirements for other ancillary inputs [32]. The LPDR *PWV* represents the total amount of water vapor in the atmospheric column within the satellite sensor field-of-view (FOV). The LPDR *PWV* algorithms were previously calibrated using the AIRS *PWV* record [31]. The LPDR *VOD* term is a negative natural logarithm of the vegetation transmissivity (Γ) to land surface microwave emissions and is frequency dependent. The LPDR data are projected to a consistent 25-km resolution global Equal-Area Scalable Earth Grid (EASE-Grid v1) projection [30].

In the LPDR algorithms, an iterative procedure is used for estimating *PWV* and the effective surface temperature (T_s) derived from 18 GHz T_b observations [30,32]. The resulting T_s is an intermediate output representing the physical temperature of the media within the effective microwave penetration depth [30]. Daily T_{mx} and T_{mn} are then estimated from the corresponding ascending (1:30 p.m.) and descending (1:30 a.m.) orbit T_s estimates, based on empirical relationships developed between T_s and daily surface air temperature measurements from the global weather station network [30]. Previous LPDR accuracy assessments indicated RMSE performance levels within 4.98 mm for *PWV* and 3.46 °C for T_{mx} and T_{mn} [32]. More detailed descriptions of the LPDR algorithms are provided elsewhere [32].

The LPDR (version 2.0) dataset used for this study was derived from a consistent, calibrated global T_b record encompassing the AMSR-E (2002–2011) and AMSR2 (2012–2017) periods of record [32]. For this investigation, the LPDR daily outputs for T_s (°C), *PWV (mm)*, *fw* (dimensionless), and Γ (dimensionless) were used for global estimation of daily VPD dynamics for selected years 2010 and 2013, which represent AMSR-E and AMSR2 portions of record, respectively. No weather station measurements were used in the LPDR algorithm for estimating T_s, *PWV*, or Γ. Here, VPD was derived

on a per grid cell basis for all land areas ($fw < 0.5$) under non-frozen conditions [38] and with minimal June, July, and August (RFI) detected, consistent with the other LPDR parameters. The VPD record was also derived in the same 25-km resolution global EASE-grid projection format as the LPDR.

2.2. ISH Record

The NCDC Integrated Surface Data (ISD) is composed of hourly and synoptic (3-hourly) weather observations from over 35,000 stations worldwide, including more than 14,000 stations being actively updated (https://www.ngdc.noaa.gov/). Most stations are distributed over North America, Europe, Australia, and parts of Asia [39]. The AMSR VPD algorithm from this study was developed and validated based on ISD hourly station observations (ISH) of surface air temperature and dew-point temperature representing the AMSR satellite observation times. Three independent sets of weather station observations, each representing 67 global stations, were used for algorithm development and validation of the AMSR VPD retrievals over the two selected study years (2010 and 2013). For each of the 67 weather stations in each ISD validation set, stations were selected to represent the major global land cover classes defined by a MODIS (MCD12C1) global International Geosphere-Biosphere Programme (IGBP) land cover classification (Figure 1) [40]. Considering the uneven distributions of the ISD stations and different spatial scales represented by station and satellite measurements, the sites were selected to ensure that their numbers were proportional to the global areal coverage of the land cover classes. The stations were also selected to represent relatively homogeneous land cover areas within the overlying 25-km resolution EASE-grid cells, following previous AMSR LPDR validation studies [30,31]. For a given year, the stations were also required to have year-long (more than 360 days) and high-quality (quality flag indicating quality check passed) measurements within ±30 min of the satellite observation time. The weather station records used for training the VPD algorithm (Section 3.2) were independent of both validation datasets, with no overlapping stations. The two validation datasets were also relatively distinct from each other due to limited stations satisfying the above selection criteria and having observations covering both 2010 and 2013.

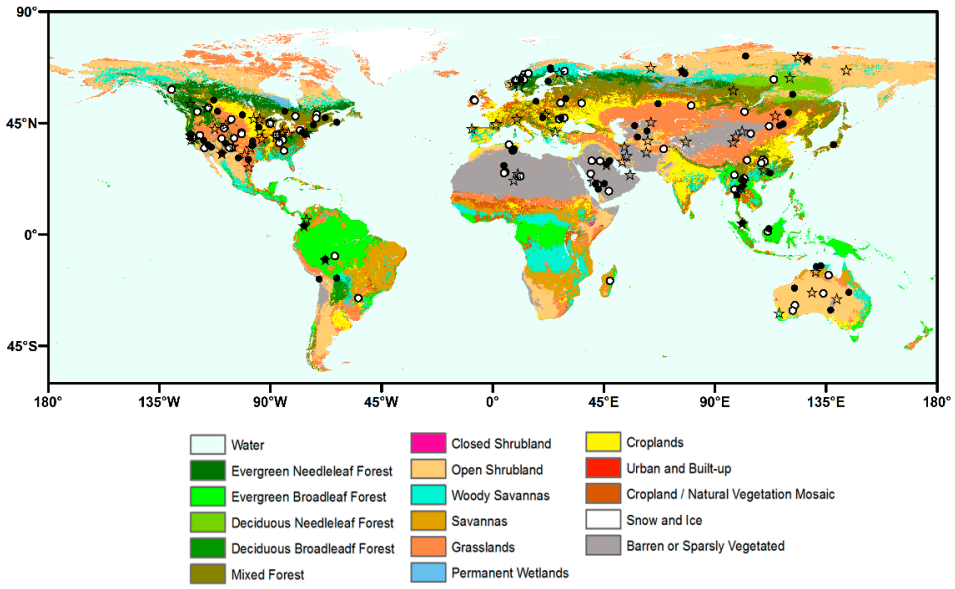

Figure 1. Locations of three sets of 67 Integrated Surface Global Hourly (ISH) stations used for algorithm training (white solid circles), and validation of Vapor Pressure Deficit (VPD) retrievals over the Advanced Microwave Scanning Radiometer for EOS (AMSR-E; 2010; black solid circles) and Advanced Microwave Scanning Radiometer 2 (AMSR2) (2013; star symbols) portions of record. Station locations are presented with the Moderate Resolution Imaging Spectroradiometer (MODIS) International Geosphere-Biosphere Programme (IGBP) land cover map.

2.3. MERRA-2 Reanalysis

MERRA-2 is the latest atmospheric reanalysis produced by the NASA Global Modeling and Assimilation Office (GMAO), which is an improvement over the original MERRA by integrating new advancements in the assimilation system [17,41,42]. In previous studies, VPD from the original MERRA showed strong correspondence (correlation coefficient (R) = 0.83) with measurements from global WMO weather stations [16]. The MERRA air temperatures were used to evaluate high-latitude freeze/thaw state distributions and trends [43,44]; and MERRA land temperatures were also applied to the development of global soil moisture and carbon products from the NASA Soil Moisture Active Passive (SMAP) mission [16]. In MERRA-2, the precipitation falling on the land surface is corrected with observations [45], which results in better land surface hydrology and energy estimates than in the original MERRA product [46,47]. Note that MERRA-2 uses only precipitation and surface pressure measurements from weather stations on land, but not surface (2-m) air temperature or humidity measurements.

In this study, the gridded ($0.5^\circ \times 0.625^\circ$) hourly surface air temperature (T_a) and dew-point temperature (T_d) at the satellite overpass times were extracted from the MERRA-2 diagnostics [34] and used to derive daily surface VPD records for each study year. The global distribution of MERRA-2 VPD was then used to evaluate the corresponding AMSR VPD results. The independent MERRA-2 and AMSR VPD records were quantitatively compared against each other and the ISH global weather station based VPD measurements over the 2010 and 2013 study years.

3. Methods

3.1. Theoretical Basis

The VPD calculation relies on the determination of the saturation vapor pressure e_s at a given air temperature T_a and the actual vapor pressure e_a as shown in Equation (1) [48]. For this study, the VPD (kPa), e_s (kPa), e_a (kPa), and T_a (°C) are defined at a standard 2-m screen-height level.

$$\mathrm{VPD} = e_s(T_a) - e_a \tag{1}$$

The dependence of e_s on T_a is theoretically described by the Clausius-Clapeyron relationship and normally approximated by the Magnus formula in applications [49]. The approximation adopted in this study has uncertainty within ±1 Pa for air temperatures extending up to 35 °C [50]:

$$e_s(T_a) = 0.611 \cdot [\exp(17.27 \cdot \frac{T_a}{T_a + 237.3})] \tag{2}$$

Similarly, e_a was calculated as the saturation vapor pressure at dew-point temperature T_d (°C), as shown in Equation (3) [22,50].

$$e_a = 0.611 \cdot [\exp(17.27 \cdot \frac{T_d}{T_d + 237.3})] \tag{3}$$

Both T_a and T_d are commonly measured by standard weather stations associated with the ISH, and also estimated by MERRA-2. Accordingly, Equations (1)–(3) were used to derive VPD from the both ISH and MERRA-2 data.

3.2. AMSR VPD Calculation

The AMSR VPD was empirically estimated using VPD observations from the global ISH training sites (Figure 1) and LPDR outputs related to surface air temperature and humidity. In order to determine VPD, regression analyses were first completed for e_s and e_a using AMSR LPDR parameters, surface elevation (H), and corresponding ISH training data. The H (km) was obtained from a global 25-km resolution digital elevation map (DEM) [35] and used as an additional ancillary input.

Considering the strong correspondence with surface air temperature (Section 2.1), the LPDR T_s was selected as the main parameter for inferring T_a along with other parameters including Γ, fw, H, and the absolute value of geographic latitude Lat (radian), similar to a previous study [32] and as shown in Equations (4) and (5). The $e_s(T_a)$ was then obtained using the estimated T_a and Equation (2). The empirical relationships in Equations (4) and (5) were derived for respective AMSR ascending (~1:30 p.m.) and descending (~1:30 a.m.) passes.

$$T_{aPM} = 7.20 + 0.91T_s - 20.88\Gamma + 19.06\Gamma^2 + 9.99\ln(fw + 1.0) - 1.43H - 0.002Lat \quad (4)$$

$$T_{aAM} = 4.46 + 0.82T_s - 7.29\Gamma + 12.41\Gamma^2 + 21.77\ln(fw + 1.0) - 0.34H - 0.001Lat \quad (5)$$

The AMSR brightness temperature retrievals at 18 to 23 GHz are sensitive to the PWV of the total air column within the sensor FOV, rather than just near-surface humidity [31]. However, previous studies based on in-situ measurements [51] and optical-IR remote sensing observations [22,24,52] demonstrated the feasibility of estimating e_a or T_d from PWV. As described in the previous studies [51–53], the linear formula in Equation (6) was used to describe the relationships between PWV and surface air humidity.

$$PWV = \frac{p_0 r_0}{g(\lambda + 1)} \quad (6)$$

where p_0 is the surface atmospheric pressure, r_0 is the surface mixing ratio, g is the acceleration of gravity and λ is a parameter related to the atmospheric moisture profile that was empirically defined using sounding measurements for the four seasons and for zones encompassing every 10 degrees of latitude over the Northern Hemisphere [51]. In this study, a second degree polynomial function, in Equation (7), was found suitable to describe the relationships between the mean absolute latitude (Lat in radians) of each zone and the corresponding λ values obtained from the literature [51], based on a favorable coefficient of determination (R^2 = 0.73) despite seasonal variations in atmospheric profiles.

$$\lambda = -1.3089Lat^2 + 1.157Lat + 2.7878 \quad (7)$$

Based on Equations (6) and (7), the PWV from the AMSR LPDR was used as the major factor for inferring e_a, as shown in Equations (8) and (9).

$$e_{aPM} = 0.18 + \left(0.0002Lat^2 - 0.0083Lat + 0.058\right)PWV \quad (8)$$

$$e_{aAM} = 0.17 - \left(0.0069Lat^2 + 0.0017Lat - 0.056\right)PWV \quad (9)$$

According to the relationships for calculating e_a and e_s (Equations (2), (4), (5), (8), and (9)), the AMSR VPD record was derived using empirical regressions between the in situ ISH VPD observations (Figure 1) and the corresponding AMSR LPDR parameters for T_s, Γ, PWV, fw, and the ancillary inputs for H and Lat (Equations (10) and (11)). The final regression forms of the retrieval algorithms (Equations (10) and (11)) account for the possible effects of terrain, vegetation [24,53], geo-location [51], and water body cover [33] on both surface air temperature and humidity. Here, the vegetation parameter Γ also partially accounts for the influence of vegetation variability and phenology on VPD.

$$\mathrm{VPD_{PM}} = 0.13 + 0.66\mathrm{e_{s0}} - 1.45\Gamma + 2.50\Gamma^2 - 0.11H - 2.21fw - (0.02Lat + 0.02)PWV \quad (10)$$

$$\mathrm{VPD_{AM}} = -0.52 + 0.59\mathrm{e_{s0}} + 0.88\Gamma + 1.00\Gamma^2 + 0.04H - 3.23fw + (0.01Lat - 0.02)PWV \quad (11)$$

where

$$e_{s0} = 0.611 \cdot \exp\left(17.27 \cdot \frac{T_s}{T_s + 237.3}\right)$$

Based on Equations (10) and (11), the twice daily global VPD estimates were generated from the LPDR for respective AMSR ascending (p.m.) and descending (a.m.) overpasses over the two study years. The availability of the AMSR VPD retrievals is consistent with the availability of the regression inputs from the LPDR, where no retrievals are performed under sub-optimal conditions, including frozen soil, severe precipitation, RFI, and snow cover [33].

The resulting AMSR VPD retrieval accuracy was evaluated against concurrent VPD measurements from the ISH weather stations (Section 2.2; Figure 1). The assessments were completed for both the global domain and major IGBP land cover classes. The statistical metrics used for the AMSR VPD accuracy assessment included bias, correlation coefficient (R), Anomaly Correlation Coefficient (ACC), Root Mean Squared Error (RMSE), and relative RMSE (rRMSE) defined as the RMSE normalized by the mean of the ISH station VPD value. The ACC is the correlation between the VPD anomalies calculated by the original VPD values after subtracting their monthly mean. In addition, the AMSR VPD accuracy is determined by the degrees to which the e_s and e_a components can be represented by the input variables H, T_s, Γ, fw, Lat, and PWV in the regressions. The regression and accuracy assessment of the component e_s and e_a variables are also used for further analysis of the resulting AMSR VPD performance.

4. Results

4.1. AMSR Global VPD Mapping

Global distributions of annual mean VPD for the AMSR p.m. (Figure 2a) and a.m. (Figure 3a) orbits were compared with corresponding MERRA-2 results for the 2010 portion of record (Figures 2b and 3b). Both products show generally similar VPD spatial patterns, which highlight the complex distributions of atmospheric moisture and heat over the global land area. Both products demonstrate a general decrease in VPD with increasing latitude, especially for the Northern Hemisphere, due to less evapotranspiration potential and cooler temperatures with lower moisture holding capacity. Higher VPD estimates from both AMSR and MERRA-2 occurred in arid and semi-arid areas including Mongolia, central Asia, the Arabian Peninsula, Sahara Desert, the Western U.S., and Northern Mexico. These regions have characteristic conditions of dry air and/or high temperatures that promote VPD extremes. In contrast, tropical rainforests have overall moderate to low VPD levels, due to ample precipitation and humid conditions in these regions, despite relatively high temperatures. In Australia, the VPD levels generally decrease along a regional moisture gradient from western and central arid regions to other parts of the country receiving greater precipitation [54]. Major differences between the MERRA-2 and AMSR VPD results occurred in arid and semi-arid areas with overall high VPD values, and in tropical rainforests where the AMSR VPD is larger (drier) than MERRA-2 VPD, except over the Mekong River basin (Figures 2c and 3c). Larger VPD differences also occurred in coastal areas due to AMSR detection of higher humidity levels near coastlines, as well as larger AMSR retrieval uncertainty for grid cells with higher surface water cover [31,32]. Compared with the p.m. estimates (Figure 2), the a.m. results (Figure 3) of both products exhibited similar spatial patterns but with much lower VPD levels. The lower a.m. VPD levels were expected considering generally cooler early morning temperatures and relatively more stable water vapor conditions throughout the day [55].

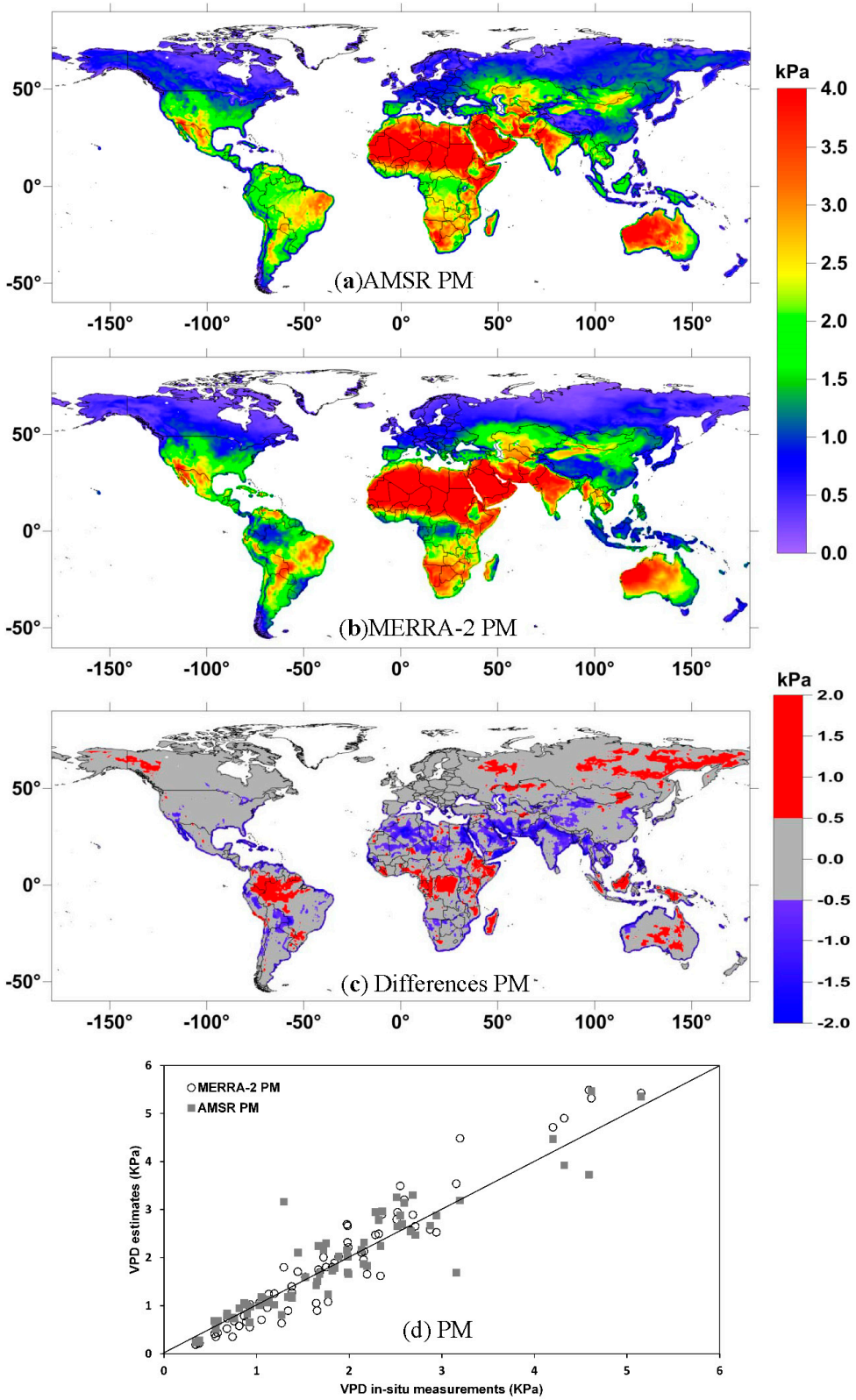

Figure 2. Mean annual Vapor Pressure Deficit (VPD) at ~1:30 p.m. local time derived from (**a**) the Advanced Microwave Scanning Radiometer (AMSR) and (**b**) the Modern-Era Retrospective analysis for Research and Applications, Version 2 (MERRA-2) reanalysis data over 2010; (**c**) the resulting VPD differences (AMSR minus MERRA-2), and (**d**) their comparisons with Integrated Surface Global Hourly (ISH) in-situ measurements.

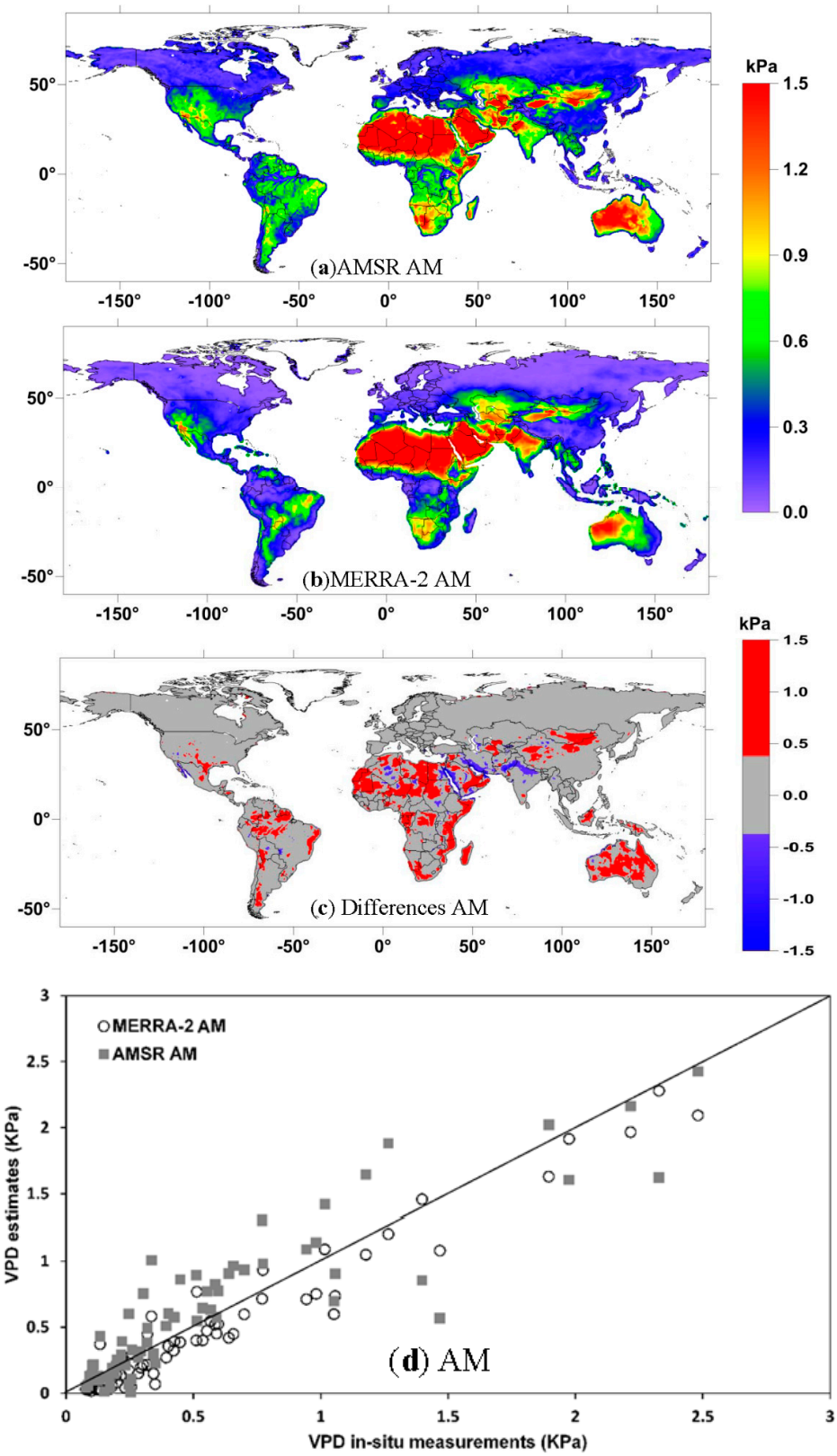

Figure 3. Mean annual Vapor Pressure Deficit (VPD) at ~1:30 a.m. local time derived from (**a**) the Advanced Microwave Scanning Radiometer (AMSR)and (**b**) the Modern-Era Retrospective analysis for Research and Applications, Version 2 (MERRA-2) reanalysis data over 2010; (**c**) the resulting VPD differences (AMSR minus MERRA-2), and (**d**) their comparisons with Integrated Surface Global Hourly (ISH) in-situ measurements.

4.2. Quantitative Comparisons between AMSR and ISH VPD

To further evaluate the VPD retrievals, quantitative comparisons were made among the AMSR, MERRA-2, and ISH VPD datasets for the two sets of 67 globally distributed validation sites (Figure 1). The time series of the VPD p.m. estimates over the selected 2010 study year were compared over the global domain and within four major IGBP land cover classes: evergreen needle leaf forest (ENF), evergreen broadleaf forest (EBF), grassland (GRS), and barren to sparsely vegetated land (BSV) (Figure 4). The selected land cover types are associated with different climate and vegetation conditions. ENF areas predominantly occur in northern high latitude boreal regions with a cold climate, EBF areas are associated with relatively hot and humid tropical climates, and GRS and BSV areas predominantly occur in semi-arid and arid environments where ecosystems are more directly affected by VPD than precipitation [14].

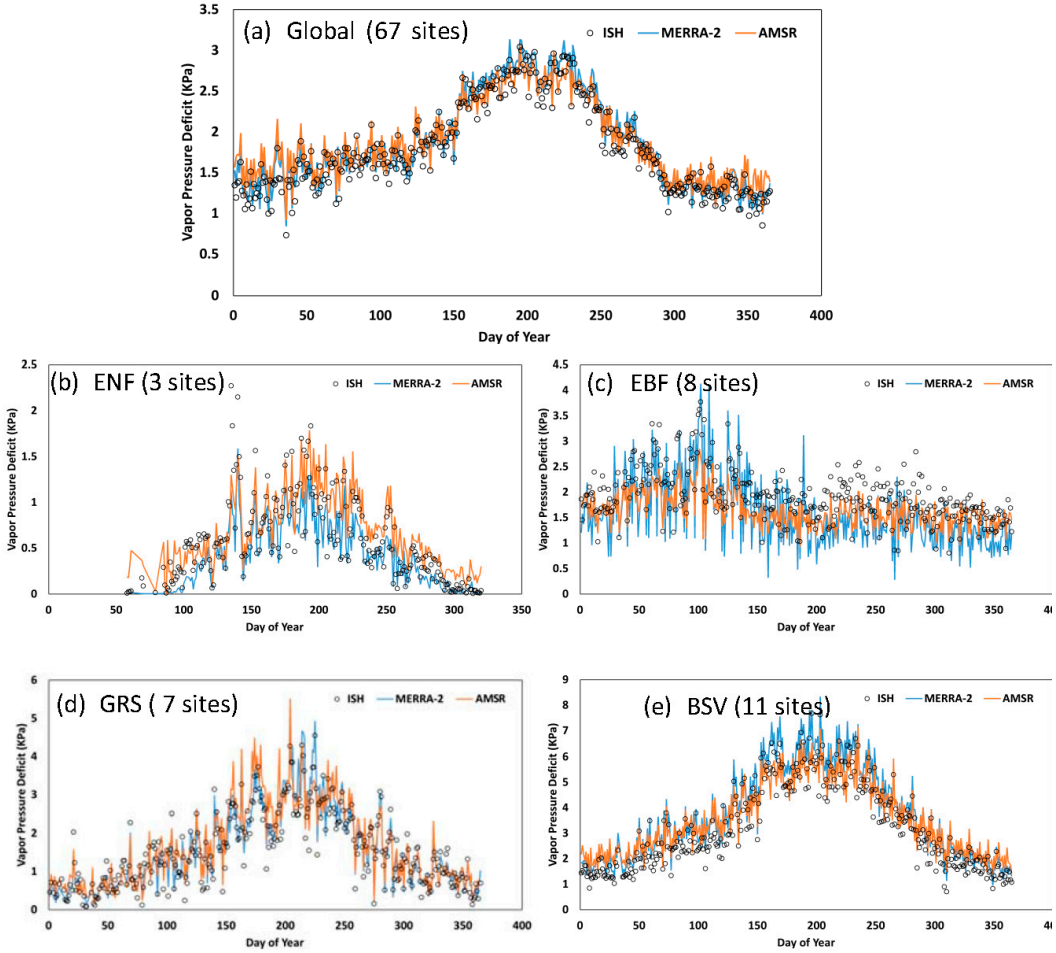

Figure 4. Afternoon (~1:30 p.m. local time) site-averaged Vapor Pressure Deficit (VPD) time series derived from respective the Advanced Microwave Scanning Radiometer (AMSR) Land Parameter Data Record (LPDR) outputs, the Modern-Era Retrospective analysis for Research and Applications, Version 2 (MERRA-2) reanalysis and Integrated Surface Global Hourly (ISH) in-situ measurements over (**a**) the globe and for major land cover types, including (**b**) evergreen needle leaf forest (ENF), (**c**) evergreen broadleaf forest (EBF), (**d**) grassland (GRS), and (**e**) barren to sparsely vegetated land (BSV) land areas over 2010.

The AMSR VPD results show clear seasonal variations and daily fluctuations for all of the land cover classes that are similar to both MERRA-2 outputs and ISH measurements (Figures 4 and 5). The p.m./a.m. standard deviations of the AMSR VPD time series are 0.48/0.14 kPa for the global, 0.40/0.11 kPa for ENF, 0.33/0.18 kPa for EBF, 1.04/0.35 kPa for GRS, and 1.40/0.50 kPa for BSV,

respectively. For ISH VPD data, the corresponding standard deviations are 0.57/0.22 kPa for the global, 0.45/0.10 kPa for ENF, 0.50/0.10 kPa EBF, 0.96/0.26 kPa for GRS, and 1.64/0.83 kPa for BSV. Except for EBF, the peak VPD levels generally appeared over the summer season months of June, July, and August (JJA) in the Northern Hemisphere, where a majority of the validation sites are located. The EBF validation sites are distributed over Amazonia and Southeast Asia, both of which have substantial tropical rainforest but different climate patterns and seasonal dry-wet periods [56,57]. Here, the time series (Figure 4c) reflect collective VPD dynamics of the EBF sites, which exhibit small seasonal variation relative to higher latitude sites. In contrast to forests (Figure 4b,c), the amplitudes of VPD seasonal cycles for GRS and BSV are relatively large, due to the predominance of continental climate conditions with greater annual temperature variations for these sites. Compared with the p.m. results (Figure 4), the a.m. VPD time series of all three datasets (Figure 5) show much lower VPD levels and less pronounced seasonality. In particular, cooler early-morning temperatures promote low a.m. VPD levels for ENF throughout the year, with annual means of all three datasets that are less than 0.11 kPa for these sites. Accordingly, the ENF VPD morning retrievals tend to have degraded signal-to-noise ratios and more variable temporal patterns (Figure 5b).

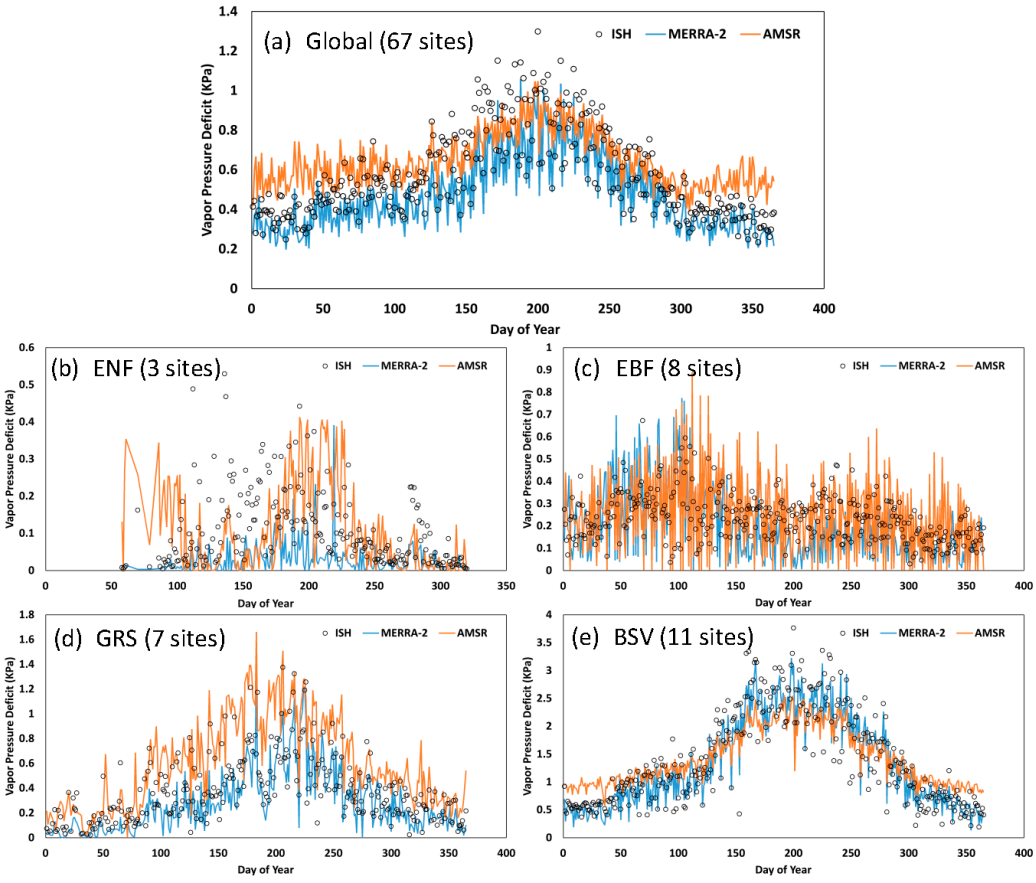

Figure 5. Morning (~1:30 a.m. local time) site-averaged Vapor Pressure Deficit (VPD) time series derived from respective the Advanced Microwave Scanning Radiometer (AMSR) Land Parameter Data Record (LPDR) outputs, the Modern-Era Retrospective analysis for Research and Applications, Version 2 (MERRA-2) reanalysis, and Integrated Surface Global Hourly (ISH) in-situ measurements over (**a**) the globe and the major land cover types, including (**b**) evergreen needle leaf forest (ENF), (**c**) evergreen broadleaf forest (EBF), (**d**) grassland (GRS), and (**e**) barren to sparsely vegetated land (BSV) land areas over 2010.

The complete VPD comparisons over the validation sites for 2010 representing the AMSR-E observation period are summarized in Tables 1 and 2 for respective p.m. and a.m. results. Both AMSR and MERRA-2 p.m. VPD estimates (Table 1) show similarly strong correspondence with the ISH station

measurements ($0.77 \leq R \leq 0.94$ for AMSR; $0.68 \leq R \leq 0.97$ for MERRA-2). The AMSR p.m. results also have an overall similar bias (0.07 kPa) but slightly higher RMSE (0.69 kPa) and rRMSE (36%) than MERRA-2 (bias 0.07 kPa; RMSE 0.63 kPa; rRMSE 33%). The performance of AMSR and MERRA-2 VPD estimates also varied by land cover class. The AMSR VPD results showed similar or better accuracy than MERRA-2 for moderately to densely vegetated areas in terms of correlations and RMSE relative to the ISH observations; whereas the opposite was true for barren to sparsely vegetated land. The ACC values for both MERRA-2 and AMSR results ($0.73 \leq$ ACC ≤ 0.92 for AMSR; $0.62 \leq$ ACC ≤ 0.97 for MERRA-2) were generally slightly smaller than the corresponding *R* statistics but still showed the prediction skills of VPD after seasonal effects were removed. For the overall results (Tables 1 and 2), which were calculated using all selected stations distributed across the globe, the similarly high AMSR ACC and *R* values indicated that the global VPD patterns related to different land cover classes are well detected by the algorithm.

Table 1. Summary of the accuracy of daily afternoon (~1:30 p.m.) Vapor Pressure Deficit (VPD) levels derived from respective the Modern-Era Retrospective analysis for Research and Applications, Version 2 (MERRA-2) and the Advanced Microwave Scanning Radiometer (AMSR) Land Parameter Data Record (LPDR) datasets for 2010 and 2013 in relation to in situ Integrated Surface Global Hourly (ISH) station measurements from 67 global validation sites. The best performance of each metric is highlighted in bold.

Land Cover [#]	Sites [#]	Obs. [#]	*R* [#]	ACC [#]	Bias (kPa)	RMSE [#] (kPa)	rRMSE [#] (%)
MERRA-2/AMSR (2010 representing AMSR-E period)							
ENF	3	648	**0.86**/**0.86**	0.78/**0.84**	−0.15/**0.11**	0.31/**0.29**	52%/**47%**
EBF	8	1599	0.68/**0.77**	0.62/**0.73**	**−0.23**/−0.25	0.84/**0.61**	43%/**31%**
DNF	1	174	0.80/**0.84**	0.74/**0.82**	−0.34/**0.12**	0.54/**0.41**	52%/**39%**
DBF	1	248	0.88/**0.94**	0.82/**0.89**	**0.02**/−0.18	0.54/**0.38**	39%/**28%**
MF	4	978	0.88/**0.90**	0.81/**0.85**	−0.15/**0.11**	0.36/**0.31**	43%/**37%**
SHR	15	3323	**0.96**/0.91	**0.97**/0.92	**0.08**/0.09	**0.53**/0.74	**26%**/36%
WSAV	5	1116	0.89/**0.94**	0.81/**0.90**	−0.20/**−0.17**	0.84/**0.56**	38%/**25%**
SAV	1	221	0.81/**0.87**	0.80/**0.87**	0.71/**0.17**	1.02/**0.53**	52%/**27%**
GRS	7	1553	**0.94**/0.89	**0.90**/0.81	**0.08**/0.18	**0.41**/0.58	**24%**/34%
CRO	8	1988	**0.87**/0.85	**0.78**/0.76	**0.01**/0.03	**0.44**/0.51	**44%**/49%
UB	1	179	0.88/**0.93**	0.71/**0.85**	−0.63/**−0.46**	0.85/**0.61**	68%/**48%**
CNVM	2	512	**0.91**/**0.91**	**0.87**/**0.87**	**0.00**/−0.11	**0.40**/0.41	**32%**/33%
BSV	11	2651	**0.97**/0.90	**0.94**/0.82	0.55/**0.34**	**0.82**/1.06	**25%**/32%
Overall	67	15190	**0.94**/0.91	**0.94**/0.91	**0.07**/**0.07**	**0.63**/0.69	**33%**/36%
MERRA-2/AMSR (2013 representing AMSR2 period)							
ENF	3	707	0.87/**0.90**	0.81/**0.86**	−0.29/**−0.23**	0.48/**0.42**	63%/**55%**
EBF	8	1524	0.67/**0.70**	0.65/**0.69**	−0.16/**−0.14**	0.78/**0.63**	**50%**/40%
DNF	1	176	0.90/**0.92**	0.87/**0.91**	**−0.06**/−0.23	**0.36**/0.41	**32%**/37%
DBF	1	216	0.85/**0.93**	0.81/**0.86**	**0.15**/0.18	0.38/**0.29**	49%/**38%**
MF	4	817	0.87/**0.90**	0.81/**0.86**	−0.15/**0.02**	0.44/**0.37**	44%/**37%**
SHR	15	2671	**0.97**/0.95	**0.97**/0.95	−0.15/**−0.07**	**0.50**/0.67	**27%**/35%
WSAV	5	1171	**0.94**/0.92	**0.93**/0.91	0.20/**−0.12**	0.68/**0.61**	34%/**31%**
SAV	1	182	0.78/**0.88**	0.80/**0.84**	**−0.50**/−0.64	1.08/**0.89**	27%/**23%**
GRS	7	1471	**0.93**/0.92	**0.88**/0.87	0.26/**0.14**	0.59/**0.56**	32%/**30%**
CRO	8	1681	0.84/**0.88**	0.72/**0.75**	0.11/**−0.03**	0.50/**0.40**	49%/**38%**
UB	1	223	0.89/**0.94**	0.80/**0.83**	**0.03**/**−0.03**	0.39/**0.28**	39%/**28%**
CNVM	2	433	0.81/**0.88**	0.70/**0.78**	0.09/**−0.06**	0.45/**0.32**	54%/**39%**
BSV	11	2247	**0.94**/0.88	**0.89**/0.81	0.18/**−0.10**	**0.71**/0.95	**22%**/30%
Overall	67	13519	**0.94**/0.92	**0.93**/0.92	**0.01**/−0.07	**0.60**/0.64	**33%**/35%

[#] ENF—Evergreen Needleleaf forest; EBF—Evergreen Broadleaf forest; DNF—Deciduous Needleleaf forest; DBF—Deciduous Broadleaf forest; MF—Mixed Forest; SHR—Shrublands; WSAV—Woody savannas; SAV—Savannas; GRS—grassland; CRO—Croplands, UB—Urban and built-up; CNVM—Cropland/Natural vegetation mosaic; and BSV—Barren to sparsely vegetated; *R* is the correlation coefficient; ACC is Anomaly Correlation Coefficient; RMSE is the Root Mean Square Error; rRMSE is the relative RMSE, which is the RMSE normalized by mean values of the ISH measured data.

Table 2. Summary of the accuracy of daily morning (~1:30 a.m.) Vapor Pressure Deficit (VPD) levels derived from respective the Modern-Era Retrospective analysis for Research and Applications, Version 2 (MERRA-2) and the Advanced Microwave Scanning Radiometer (AMSR) Land Parameter Data Record (LPDR) datasets for 2010 and 2013 in relation to in situ Integrated Surface Global Hourly (ISH) station measurements from 67 global validation sites. The best performance of each metric is highlighted in bold.

Land Cover [#]	Site [#]	Obs. [#]	*R* [#]	ACC [#]	Bias (kPa)	RMSE [#] (kPa)	rRMSE [#] (%)
MERRA-2/AMSR (2010 representing AMSR-E period)							
ENF	3	607	0.19/**0.28**	0.11/**0.22**	−0.08/**−0.01**	**0.15**/0.16	**133%**/135%
EBF	8	1614	**0.41**/0.32	**0.37**/0.27	**−0.02**/0.06	**0.30**/0.31	**123%**/130%
DNF	1	150	−0.04/**0.07**	−0.09/**−0.05**	**−0.05**/0.11	**0.16**/0.24	**155%**/231%
DBF	1	242	**0.48**/0.46	**0.42**/0.34	−0.13/**−0.01**	**0.28**/0.29	**100%**/102%
MF	4	950	0.21/**0.48**	0.20/**0.49**	−0.11/**−0.03**	0.20/**0.19**	135%/**124%**
SHR	15	3086	**0.89**/0.77	**0.89**/0.78	−0.17/**0.07**	**0.42**/0.54	**55%**/72%
WSAV	5	1200	0.66/**0.67**	**0.50**/0.46	**−0.11**/**0.11**	0.43/**0.40**	83%/**78%**
SAV	1	214	**0.66**/0.38	**0.42**/0.22	0.25/**0.03**	0.47/**0.39**	91%/**76%**
GRS	7	1512	**0.66**/0.56	**0.55**/0.37	**−0.10**/0.26	**0.31**/0.45	**73%**/105%
CRO	8	1775	0.56/**0.63**	0.49/**0.59**	−0.06/**0.05**	0.22/**0.21**	101%/**97%**
UB	1	236	0.37/**0.62**	0.05/**0.16**	−0.28/**−0.12**	0.36/**0.24**	104%/**70%**
CNVM	2	493	0.47/**0.54**	0.40/**0.48**	−0.08/**0.06**	0.24/**0.22**	86%/**79%**
BSV	11	2527	**0.91**/0.80	**0.85**/0.69	−0.08/**0.05**	**0.53**/0.78	**37%**/54%
Overall	67	14606	**0.90**/0.82	**0.89**/0.81	−0.10/**0.07**	**0.37**/0.48	**63%**/80%
MERRA-2/AMSR (2013 representing AMSR2 period)							
ENF	3	642	**0.29**/0.22	**0.23**/0.14	−0.14/**−0.07**	0.23/**0.22**	133%/**123%**
EBF	8	1492	**0.32**/0.15	**0.31**/0.12	−0.07/**0.05**	**0.26**/0.32	**121%**/153%
DNF	1	156	0.17/**0.29**	0.04/**0.26**	**−0.10**/−0.18	**0.32**/**0.32**	**124%**/125%
DBF	1	208	0.23/**0.24**	**0.23**/0.08	−0.13/**−0.01**	**0.19**/0.24	**102%**/125%
MF	4	762	0.10/**0.42**	0.05/**0.36**	−0.08/**0.06**	**0.22**/0.25	**130%**/149%
SHR	15	2474	**0.89**/0.82	**0.89**/0.82	−0.23/**−0.08**	**0.51**/0.58	**63%**/71%
WSAV	5	1059	**0.72**/**0.72**	0.70/**0.71**	−0.16/**−0.09**	0.45/**0.42**	76%/**71%**
SAV	1	181	**0.58**/0.47	0.11/**0.17**	**−0.04**/0.23	**0.58**/0.60	**60%**/62%
GRS	7	1424	**0.76**/0.66	**0.68**/0.54	**−0.06**/0.27	**0.30**/0.45	**62%**/93%
CRO	8	1596	0.40/**0.52**	0.31/**0.41**	**−0.06**/0.09	**0.24**/0.26	**107%**/119%
UB	1	199	0.56/**0.62**	**0.48**/0.43	−0.20/**0.04**	0.28/**0.22**	90%/**70%**
CNVM	2	359	0.20/**0.35**	0.21/**0.31**	−0.03/**0.02**	**0.24**/**0.24**	**127%**/130%
BSV	11	2162	**0.82**/0.70	**0.69**/0.60	−0.27/**−0.02**	**0.72**/0.82	**49%**/56%
Overall	67	12714	**0.87**/0.80	**0.86**/0.80	−0.15/**0.02**	**0.44**/0.50	**72%**/82%

[#] ENF—Evergreen Needleleaf forest; EBF—Evergreen Broadleaf forest; DNF—Deciduous Needleleaf forest; DBF—Deciduous Broadleaf forest; MF—Mixed Forest; SHR—Shrublands; WSAV—Woody savannas; SAV—Savannas; GRS—grassland; CRO—Croplands, UB—Urban and built-up; CNVM—Cropland/Natural vegetation mosaic; and BSV—Barren to sparsely vegetated; *R* is the correlation coefficient; ACC is Anomaly Correlation Coefficient; RMSE is the Root Mean Square Error; rRMSE is the relative RMSE, which is the RMSE normalized by mean values of the ISH measured data.

Both AMSR and MERRA-2 a.m. VPD estimates showed lower correlations than the p.m. results as evaluated by both *R* and ACC with the ISH observations, which is partly due to the characteristic smaller a.m. VPD seasonal variations. In an extreme case, correlations with the ISH observations are very weak for the DNF sites ($R = -0.04$ for MERRA-2 and 0.07 for AMSR), where overall small VPD values lead to low RMSE (0.16KPa for MERRA-2; 0.24KPa for AMSR) but large rRMSE (155% for MERRA-2; 231% for AMSR) values. For the a.m. results, the overall AMSR VPD accuracy was slightly lower than MERRA-2 for both *R* and RMSE metrics in relation to the ISH station observations. On the other hand, the AMSR results showed similar biases (0.07 kPa) for the p.m. and a.m. retrievals, whereas MERRA-2 VPD had opposite biases for respective p.m. (0.07 kPa) and a.m. (−0.10 kPa) conditions relative to the ISH observations.

The AMSR VPD estimates for 2013 representing the AMSR2 observation period are consistent with those for 2010 and show similar error levels and correlations relative to the ISH p.m. (RMSE = 0.64 kPa, $0.70 \leq R \leq 0.95$, $0.69 \leq$ ACC ≤ 0.95, p-value < 0.001; Table 1) and a.m. (RMSE = 0.50 kPa, $0.15 \leq R \leq 0.82$, $0.08 \leq$ ACC ≤ 0.82, p-value < 0.001; Table 2) observations. The performance of the AMSR VPD record for 2013 also resembled the results for 2010 in the pattern of accuracies varying with land cover types and seasonal period. In contrast to the positive biases of the AMSR VPD estimates

for 2010 relative to the ISH observations, a wetter bias (−0.07 kPa) for p.m. and a slightly drier bias (0.02 kPa) for a.m. were found in the AMSR results for 2013. Considering the overall similar performance of the AMSR VPD retrievals for the AMSR-E (2010) and AMSR2 (2013) portions of record, the following analysis is primarily focused on the 2010 record, whereas the general consistency of the AMSR-E and AMSR2 portions of the VPD data record is discussed further in Section 5.2.

4.3. Evaluations of AMSR e_s and e_a Estimates

For evaluating discrepancies between the AMSR VPD retrievals and the ISH station observations, additional regressions were completed for the VPD components, e_s and e_a, using the AMSR LPDR outputs and ISH measurements from the training sites. The relative AMSR accuracy for e_s and e_a was evaluated against the ISH validation site observations in the 2010 record. The respective AMSR LPDR e_s p.m. and a.m. estimates showed overall high consistency with the ISH observations, including favorable correlations (R = 0.93 and 0.92), small bias (0.03 kPa and −0.01 kPa), relatively low RMSE (0.68 kPa and 0.42 kPa), and similar rRMSE (22% and 23%) levels. These results suggest a high correspondence between the LPDR T_s retrievals and surface air temperatures, which is consistent with previous studies [32]. The e_a performance was generally lower than that of e_s, as shown by decreased correlations with the ISH observations (R = 0.87 for p.m. and 0.84 for a.m. results). Similar to the LPDR *PWV* record, retrieval errors for the p.m. e_a results were relatively lower than the a.m. estimates (respective 0.38 kPa and 32% for RMSE and rRMSE for p.m.; and 0.42 kPa and 34% for a.m. results), whereas the biases were small for both p.m. (0.05 kPa) and a.m. (0.02 kPa) results. We note that VPD can also be calculated as the difference between the e_s and e_a estimates, but the corresponding accuracy (R = 0.91 and RMSE = 0.71 kPa for p.m.; and R = 0.78 and RMSE = 0.51 kPa for a.m.) was slightly lower than the results derived from Equations (10) and (11) (Tables 1 and 2). The evaluations of e_s and e_a estimates described here are therefore only used to analyze potential sources of uncertainty in the VPD retrievals as detailed in the following section.

5. Discussion

The satellite microwave remote sensing based VPD retrieval method described in this study was found overall to have favorable global performance and strong correspondence with independent in situ weather station measurements spanning a diversity of climate and vegetation conditions, though the AMSR VPD accuracy varied with satellite observation time (a.m. vs. p.m.) and for different land cover regions. The AMSR VPD results also showed similar spatial and seasonal patterns in relation to other available global VPD records from the MERRA-2 global reanalysis, but with notable differences in tropical areas. For analyzing VPD retrieval uncertainties, the LPDR performance in estimating the VPD components e_s and e_a within different land cover classes was evaluated against the corresponding ISH and MERRA-2 results.

5.1. Retrieval Uncertainties of AMSR VPD, e_s, and e_a

The correspondence between AMSR and ISH results for selected year 2010 was analyzed for VPD and the component e_s and e_a parameters over the global domain and for major land cover classes (Figure 6). A similar analysis was also conducted using the MERRA-2 outputs and ISH data (Figure 7). For the AMSR p.m. results (Figure 6a), the respective correlations with the ISH station observations for VPD,e_s, and e_a were generally consistent with each other and showed similar spatial and temporal variations for the different land cover classes. These results suggest common factors influencing all three humidity parameters. As higher-order retrievals, the AMSR VPD, e_s, and e_a retrievals were affected by underlying uncertainties in the lower-order T_b observations and LPDR outputs. For the AMSR LPDR T_s, Γ, and *PWV* parameters, a low-quality flag was assigned to the 25-km grid cells having larger expected retrieval uncertainties due to the following conditions: high vegetation biomass levels (e.g., X-band $VOD > 2.3$), saturated emission signals indicated by T_b polarization differences at 18 GHz or 23 GHz less than 1.0 K, or large water bodies occupying more than 20% of a grid cell

($fw > 0.2$) [32]. Accordingly, EBF regions were estimated to have relatively low retrieval quality for both the original LPDR (Figure 9 in Du et al. [32]) and the current VPD, e_s, and e_a results due to relatively dense forest cover in these areas. For BSV regions, the relatively low correlation of the e_a results was caused by lower humidity levels in these predominantly arid and semi-arid regions, which show relatively little temporal variability. Air temperatures played a more important role in estimating VPD in these warm, dry climate areas as evidenced by similarly high correlations of the e_s and VPD results (Figure 6). The AMSR a.m. VPD estimates showed lower correspondence with the ISH observations than the p.m. results despite strong AMSR and ISH correlations for e_s and e_a (Figure 6b). The a.m. retrieval uncertainties are magnified by the much smaller seasonal variations in early morning air temperatures and corresponding VPD values (Figure 5). Compared with the AMSR estimates, the MERRA-2 e_s and e_a data (Figure 7) showed generally stronger correlations with the ISH observations, especially for the p.m. results over moderate to sparsely vegetated areas, and for most of the a.m. results. The relatively higher MERRA-2 accuracy for these parameters also promoted overall greater VPD accuracy than the AMSR results, as shown in Tables 1 and 2.

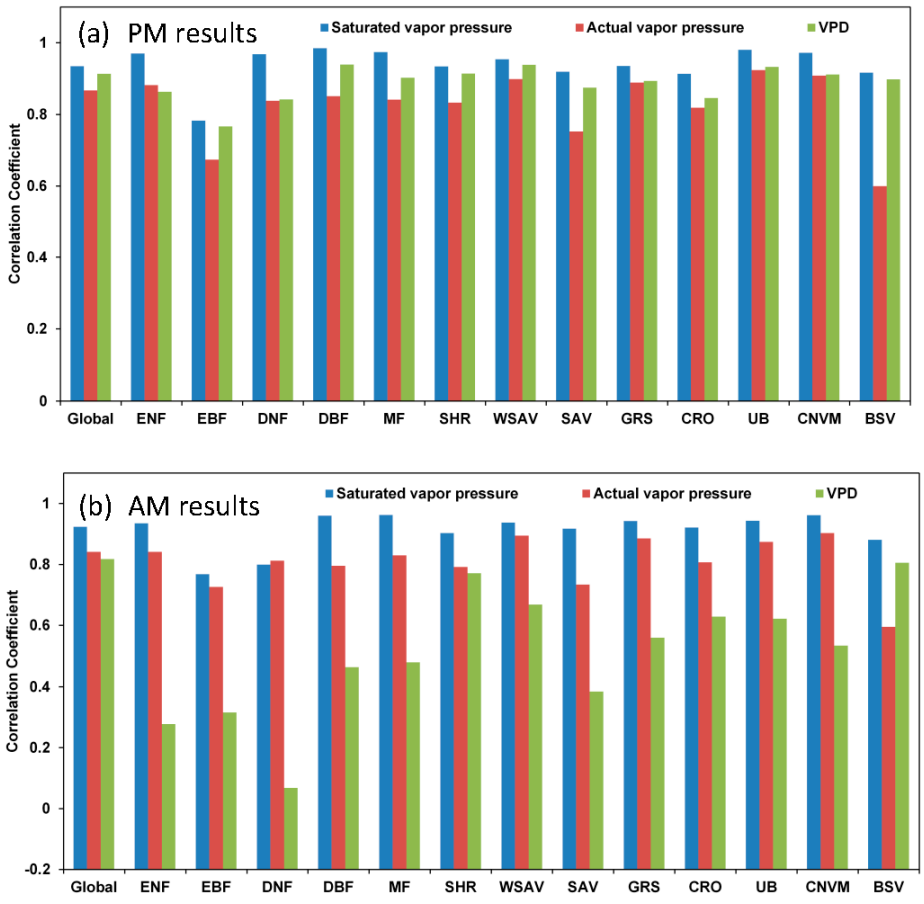

Figure 6. Correlations between the Advanced Microwave Scanning Radiometer (AMSR) Land Parameter Data Record (LPDR) (**a**) p.m. and (**b**) a.m. estimates and Integrated Surface Global Hourly (ISH) station observations of saturation vapor pressure (e_s), actual vapor pressure (e_a), and Vapor Pressure Deficit (VPD) for 2010 over the global domain and major land cover classes including ENF—Evergreen Needleleaf forest; EBF—Evergreen Broadleaf forest; DNF—Deciduous Needleleaf forest; DBF—Deciduous Broadleaf forest; MF—Mixed Forest; SHR—Shrublands; WSAV—Woody savannas; SAV—Savannas; GRS—grassland; CRO—Croplands, UB—Urban and built-up; CNVM—Cropland/Natural vegetation mosaic; and BSV—Barren to sparsely vegetated.

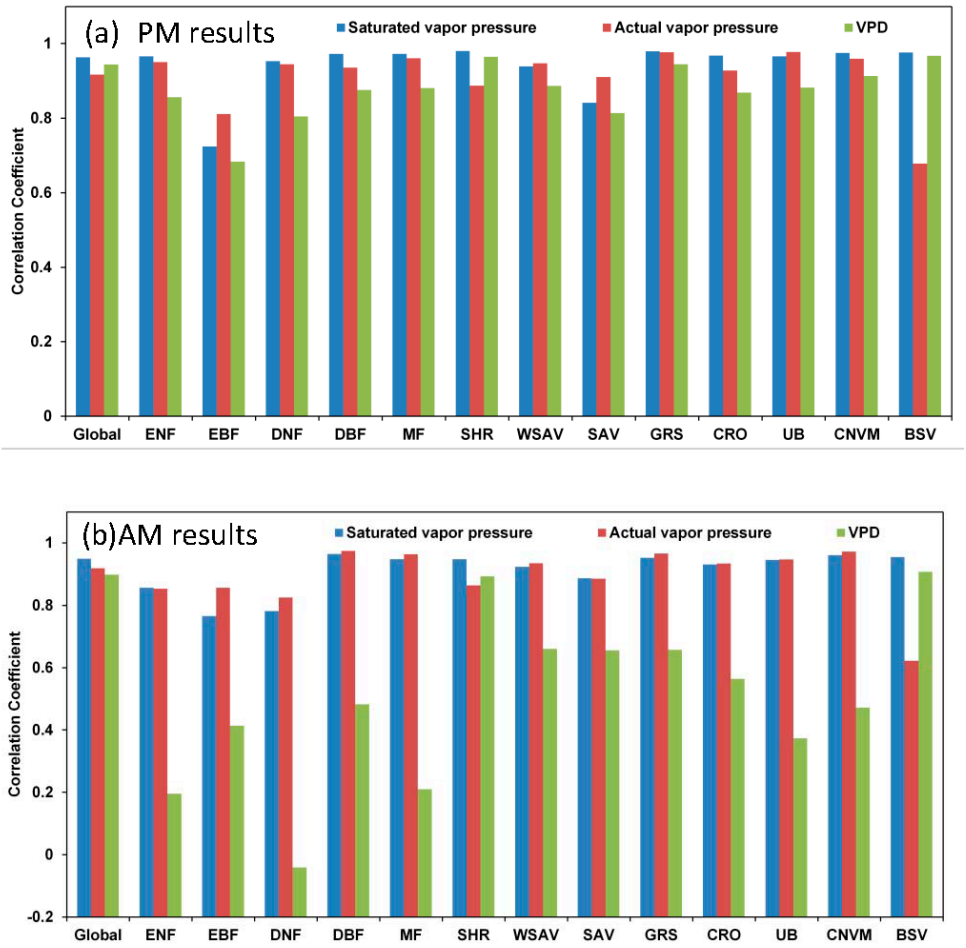

Figure 7. Correlations between the Modern-Era Retrospective analysis for Research and Applications, Version 2 (MERRA-2) (**a**) p.m. and (**b**) a.m. predictions and Integrated Surface Global Hourly (ISH) station observations of saturation vapor pressure (e_s), actual vapor pressure (e_a), and Vapor Pressure Deficit (VPD) for 2010 over the global domain and major land cover classes including ENF—Evergreen Needleleaf forest; EBF—Evergreen Broadleaf forest; DNF—Deciduous Needleleaf forest; DBF—Deciduous Broadleaf forest; MF—Mixed Forest; SHR—Shrublands; WSAV—Woody savannas; SAV—Savannas; GRS—grassland; CRO—Croplands, UB—Urban and built-up; CNVM—Cropland/Natural vegetation mosaic; and BSV—Barren to sparsely vegetated.

Both MERRA-2 and AMSR-based VPD records showed similar spatial and seasonal patterns over the global domain and different land cover classes (Figures 2–5). The MERRA-2 and AMSR datasets provide two independent estimations of regional VPD conditions at 0.5° × 0.625° and 25-km resolutions, respectively, whereas the ISH data are derived from in situ weather station measurements. Differences in the representative areas of these data records may contribute to differences in their accuracy.

5.2. Consistency of the AMSR VPD Data Record

As introduced in Section 2.1, the LPDR algorithms were initially developed for AMSR-E and later applied using similar AMSR2 T_b observations after cross-sensor calibration of the long-term AMSR-E and AMSR2 T_b records [56]. However, residual T_b biases may remain between the AMSR-E and AMSR2 portions of record, which may affect the AMSR VPD retrievals. A previous study identified AMSR2 biases in the LPDR relative to the AMSR-E portion of record for *PWV* (−0.50 mm for p.m.; −0.45 mm for a.m.), T_{mx} (−0.24 °C), and T_{mn} (0.13 °C) [30]. The VPD retrievals developed from the

available LPDR data are therefore also affected by the uncertainties originating from the cross-sensor T_b calibrations. However, the AMSR VPD assessments for the AMSR-E (2010) and AMSR2 (2013) portions of the record had similar performance and a generally consistent bias in relation to the independent ISH stations and MERRA-2 global observations. Assuming the VPD data derived from two sets of ISH validation stations were consistent, the corresponding biases of the AMSR VPD estimates for the 2013 (AMSR2) and 2010 (AMSR-E) portions of record are −0.14 kPa and −0.05 kPa for the p.m. and a.m. overpasses, respectively. Alternatively, the MERRA-2 and AMSR datasets have similar spatial scales and regional representativeness, so the AMSR VPD biases for 2013 and 2010 calculated using MERRA-2 data as a benchmark are −0.08 kPa and 0.00 kPa for the p.m. and a.m. overpass results, respectively. A more thorough analysis on the data consistency should be performed for the entire data record with the assistance of independent and consistent datasets for the globe and over the same multi-year period. Such analysis is currently limited by the lack of globally distributed stations satisfying the data selection criteria required for this study (Section 2.2).

6. Conclusions

The near-surface VPD is an important parameter governing ecological processes, yet global high-temporal repeat and moderate spatial resolution satellite VPD products suitable for landscape level studies are still lacking. Here, a new method was proposed for satellite-based global assessment and monitoring of land surface VPD dynamics at 25 km spatial resolution using AMSR passive microwave remote sensing observations. The AMSR VPD results highlighted the strong global performance and accuracy in relation to independent VPD observations from global in situ ISH weather stations. The accuracy of the AMSR VPD retrievals in relation to the in situ measurements was similar to the VPD estimates derived from the MERRA-2 global reanalysis, which benefits from a well-calibrated land model informed by extensive global observations [17,42]. The favorable AMSR VPD performance indicates its potential suitability as an observational benchmark to confront global models given that atmospheric humidity is an essential climate variable (ECV) that impacts multiple climate, energy, ecosystem, and hydrological processes.

The AMSR VPD retrievals derived from the ~1:30 p.m. overpass data was generally more accurate due to stronger seasonality and the larger magnitude of the retrievals relative to the ~1:30 a.m. results. The retrieval uncertainties also varied for different land cover classes according to the variable climate and vegetation conditions, and the underlying LPDR accuracy in representing surface air temperature and humidity. The VPD estimates were evaluated for the 2010 and 2013 period. Future studies conducted for the whole LPDR multi-year record are needed for a more thorough assessment of the data quality and consistency. The generally favorable performance from both morning and afternoon retrievals enables potential investigations of VPD diurnal variability as an influence on vegetation stress and evapotranspiration. The same VPD retrieval formulas can also be applied to the entire calibrated AMSR T_b record [58], enabling the development of a long-term (from 2002) global VPD record, with continued monitoring from ongoing AMSR2 operations. The satellite VPD estimates derived from AMSR and other complementary satellite sensors, such as AIRS, MODIS, and AVHRR, provide opportunities for evaluating regional drought patterns and other climate change related impacts on terrestrial ecosystems, while providing an observational benchmark for evaluating global climate model predictions.

Author Contributions: J.D. and J.S.K. designed the study and analyzed the data; R.H.R., L.A.J., J.D.W. and Y.K. contributed to data and analysis; all the authors contributed to the writing.

Funding: This work was conducted at the University of Montana with funding from the National Aeronautics and Space Administration (NASA) (Grant number: NNX14AB20A, NNX15AB59G). R. Reichle was supported by the NASA Modeling, Analysis and Prediction program.

Acknowledgments: AMSR-E data are produced by Remote Sensing Systems and sponsored by the NASA Earth Science MEaSUREs DISCOVER Project and the AMSR-E Science Team. Data are available at www.remss.com. AMSR-E data and land cover classification maps were also provided courtesy of the National Snow and Ice Data Center (NSIDC). The AMSR2 L1R data used for this study were provided courtesy of JAXA. The AMSR LPDR

is publicly available at NSIDC, while the VPD record developed from this study is available through NTSG (http://files.ntsg.umt.edu/data/LPDR_v2/Binary/VPD/).

Conflicts of Interest: The authors declare no conflict of interest. The founding sponsors had no role in the design of the study; in the collection, analyses, or interpretation of data; in the writing of the manuscript, and in the decision to publish the results.

References

1. Murray, F.W. On the computation of saturation vapor pressure. *J. Appl. Meteorol.* **1967**, *6*, 203–204. [CrossRef]
2. Running, S.W.; Nemani, R.R. Relating seasonal patterns of the AVHRR vegetation index to simulate photosynthesis and transpiration of forests in different climates. *Remote Sens. Environ.* **1988**, *24*, 347–367. [CrossRef]
3. Gu, L.; Meyers, T.; Pallardy, S.G.; Hanson, P.J.; Yang, B.; Heuer, M.; Hosman, K.P.; Riggs, J.S.; Sluss, D.; Wullschleger, S.D. Direct and indirect effects of atmospheric conditions and soil moisture on surface energy partitioning revealed by a prolonged drought at a temperate forest site. *J. Geophys. Res. Atmos.* **2006**, *111*. [CrossRef]
4. Day, M.E. Influence of temperature and leaf-to-air vapor pressure deficit on net photosynthesis and stomatal conductance in red spruce (*Picea rubens*). *Tree Physiol.* **2000**, *20*, 57–63. [CrossRef] [PubMed]
5. Zhao, M.; Running, S.W. Drought-induced reduction in global terrestrial net primary production from 2000 through 2009. *Science* **2010**, *329*, 940–943. [CrossRef] [PubMed]
6. Monteith, J.L. Evaporation and environment. In *The State and Movement of Water in Living Organisms*; Fogg, C.E., Ed.; Cambridge Univerity Press: Cambridge, UK, 1965; pp. 205–234.
7. Shuttleworth, W.J. Evaporation. In *Handbook of Hydrology*; Maidment, D.R., Ed.; McGraw Hill: New York, NY, USA, 1993.
8. Running, S.W.; Nemani, R.R.; Heinsch, F.A.; Zhao, M.; Reeves, M.; Hashimoto, H. A continuous satellite-derived measure of global terrestrial primary production. *Bioscience* **2004**, *54*, 547–560. [CrossRef]
9. Mu, Q.; Jones, L.A.; Kimball, J.S.; McDonald, K.C.; Running, S.W. Satellite assessment of land surface evapotranspiration for the pan-Arctic domain. *Water Resour. Res.* **2009**, *45*. [CrossRef]
10. Jones, L.A.; Kimball, J.S.; Reichle, R.H.; Madani, N.; Glassy, J.M.; Ardizzone, J.V.; Colliander, A.; Cleverly, J.; Desai, A.R.; Eamus, D.; et al. The SMAP level 4 carbon product for monitoring ecosystem land-atmosphere CO_2 exchange. *IEEE Trans. Geosci. Remote Sens.* **2017**, *55*. [CrossRef]
11. Lobell, D.B.; Roberts, M.J.; Schlenker, W.; Braun, N.; Little, B.B.; Rejesus, R.M.; Hammer, G.L. Greater sensitivity to drought accompanies maize yield increase in the US Midwest. *Science* **2014**, *344*, 516–519. [CrossRef] [PubMed]
12. Jones, M.O.; Kimball, J.S.; Small, E.E.; Larson, K.M. Comparing land surface phenology derived from satellite and GPS network microwave remote sensing. *Int. J. Biometeorol.* **2014**, *58*, 1305–1315. [CrossRef] [PubMed]
13. Williams, A.P.; Allen, C.D.; Macalady, A.K.; Griffin, D.; Woodhouse, C.A.; Meko, D.M.; Swetnam, T.W.; Rauscher, S.A.; Seager, R.; Grissino-Mayer, H.D.; et al. Temperature as a potent driver of regional forest drought stress and tree mortality. *Nat. Clim. Chang.* **2013**, *3*, 292–297. [CrossRef]
14. Konings, A.G.; Williams, A.P.; Gentine, P. Sensitivity of grassland productivity to aridity controlled by stomatal and xylem regulation. *Nat. Geosci.* **2017**, *10*, 284–288. [CrossRef]
15. Lucchesi, R. *File Specification for GEOS-5 FP (Forward Processing)*; GMAO Office Note 4 (Version 1.0); NASA: Washington, DC, USA, 2013. Available online: https://gmao.gsfc.nasa.gov/products/documents/GEOS_5_FP_File_Specification_ON4v1_0.pdf (accessed on 10 March 2018).
16. Yi, Y.; Kimball, J.S.; Jones, L.A.; Reichle, R.H.; McDonald, K.C. Evaluation of MERRA land surface estimates in preparation for the soil moisture active passive mission. *J. Clim.* **2011**, *24*, 3797–3816. [CrossRef]
17. Gelaro, R.; McCarty, W.; Suárez, M.J.; Todling, R.; Molod, A.; Takacs, L.; Randles, C.A.; Darmenov, A.; Bosilovich, M.G.; Reichle, R.; et al. The modern-era retrospective analysis for research and applications, version 2 (MERRA-2). *J. Clim.* **2017**, *30*, 5419–5454. [CrossRef]
18. Dee, D.P.; Uppala, S.M.; Simmons, A.J.; Berrisford, P.; Poli, P.; Kobayashi, S.; Andrae, U.; Balmaseda, M.A.; Balsamo, G.; Bauer, P.; et al. The ERA-interim reanalysis: Configuration and performance of the data assimilation system. *Q. J. R. Meteorol. Soc.* **2011**, *137*, 553–597. [CrossRef]

19. Kalnay, E.; Jenne, R. The NMC/NCAR 40-year reanalysis project. *Bull. Am. Meteorol. Soc.* **1996**, *77*, 437–471. [CrossRef]
20. Kistler, R.; Kalnay, E.; Collins, W.; Saha, S.; White, G.; Woollen, J.; Chelliah, M.; Ebisuzaki, W.; Kanamitsu, M.; Kousky, V.; et al. The NCEP-NCAR 50-year reanalysis: Monthly means CD-ROM and documentation. *Bull. Am. Meteorol. Soc.* **2001**, *82*, 247–268. [CrossRef]
21. Zhang, K.; Kimball, J.S.; Nemani, R.R.; Running, S.W. A continuous satellite-derived global record of land surface evapotranspiration from 1983 to 2006. *Water Resour. Res.* **2010**, *46*. [CrossRef]
22. Prince, S.D.; Goetz, S.J.; Dubayah, R.O.; Czajkowski, K.P.; Thawley, M. Inference of surface and air temperature, atmospheric precipitable water and vapor pressure deficit using advanced very high-resolution radiometer satellite observations: Comparison with field observations. *J. Hydrol.* **1998**, *212*, 230–249. [CrossRef]
23. Hashimoto, H.; Dungan, J.L.; White, M.A.; Yang, F.; Michaelis, A.R.; Running, S.W.; Nemani, R.R. Satellite-based estimation of surface vapor pressure deficits using MODIS land surface temperature data. *Remote Sens. Environ.* **2008**, *112*, 142–155. [CrossRef]
24. Zhang, H.; Wu, B.; Yan, N.; Zhu, W.; Feng, X. An improved satellite-based approach for estimating vapor pressure deficit from MODIS data. *J. Geophys. Res. Atmos.* **2014**, *119*. [CrossRef]
25. Green, R.M.; Hay, S.I. The potential of pathfinder AVHRR data for providing surrogate climatic variables across Africa and Europe for epidemiological applications. *Remote Sens. Environ.* **2002**, *79*, 166–175. [CrossRef]
26. Sahin, M.; Yildiz, B.Y.; Senkal, O.; Pestemalci, V. Estimation of the vapour pressure deficit using NOAA-AVHRR data. *Int. J. Remote Sens.* **2013**, *34*, 2714–2729. [CrossRef]
27. Susskind, J.; Blaisdell, J.M.; Iredell, L. Improved methodology for surface and atmospheric soundings, error estimates, and quality control procedures: The atmospheric infrared sounder science team version-6 retrieval algorithm. *J. Appl. Remote Sens.* **2014**, *8*. [CrossRef]
28. Levine, P.A.; Randerson, J.T.; Swenson, S.C.; Lawrence, D.M. Evaluating the strength of the land-atmosphere moisture feedback in Earth system models using satellite observations. *Hydrol. Earth Syst. Sci.* **2016**, *20*. [CrossRef]
29. Jones, L.A. Satellite Microwave Remote Sensing of Boreal-Arctic Land Surface State and Meteorology from AMSR-E. Master's Thesis, University of Montana, Missoula, MT, USA, 2007.
30. Jones, L.A.; Ferguson, C.R.; Kimball, J.S.; Zhang, K.; Chan, S.T.K.; McDonald, K.C.; Njoku, E.G.; Wood, E.F. Satellite microwave remote sensing of daily land surface air temperature minima and maxima from AMSR-E. *IEEE J. Sel. Top. Appl. Earth Obs. Remote Sens.* **2010**, *3*, 111–123. [CrossRef]
31. Du, J.; Kimball, J.S.; Jones, L.A. Satellite microwave retrieval of total precipitable water vapor and surface air temperature over land from AMSR2. *IEEE Trans. Geosci. Remote Sens.* **2015**, *53*, 2520–2531. [CrossRef]
32. Du, J.; Kimball, J.S.; Jones, L.A.; Kim, Y.; Glassy, J.; Watts, J.D. A global satellite environmental data record derived from AMSR-E and AMSR2 microwave Earth observations. *Earth Syst. Sci. Data* **2017**, *9*. [CrossRef]
33. Kimball, J.S.; White, M.A.; Running, S.W. Biome-BGC simulations of stand hydrologic processes for BOREAS. *J. Geophys. Res. Atmos.* **1997**, *102*, 29043–29051. [CrossRef]
34. *MERRA-2 tavg1_2d_slv_Nx: 2d, 1-Hourly, Time-Averaged, Single-Level, Assimilation, Single-Level Diagnostics V5.12.4*; Global Modeling and Assimilation Office (GMAO), Goddard Earth Sciences Data and Information Services Center (GES DISC): Greenbelt, MD, USA, 2015; Available online: 10.5067/VJAFPLI1CSIV (accessed on 12 April 2018).
35. Knowles, K. *EASE-Grid Elevation Data Resampled from the Global Land One-km Base Elevation (GLOBE) Project*; National Snow and Ice Data Center, Digital Media: Boulder, CO, USA, 2001.
36. Koike, T.; Nakamura, Y.; Kaihotsu, I.; Davva, G.; Matsuura, N.; Tamagawa, K.; Fujii, H. Development of an Advanced Microwave Scanning Radiometer (AMSR-E) algorithm of soil moisture and vegetation water content. *Proc. Hydraul. Eng.* **2004**, *48*, 217–222. [CrossRef]
37. Imaoka, K.; Takashi, M.; Misako, K.; Marehito, K.; Norimasa, I.; Keizo, N. Status of AMSR2 instrument on GCOM-W1, earth observing missions and sensors: Development, implementation, and characterization II. *Proc. SPIE* **2012**, *8528*, 852815.
38. Kim, Y.; Kimball, J.S.; Glassy, J.; Du, J. An extended global earth system data record on daily landscape freeze-thaw status determined from satellite passive microwave remote sensing. *Earth Syst. Sci. Data* **2017**, *9*, 133–147. [CrossRef]

39. Global Surface Hourly. *NOAA National Centers for Environmental Information*; Global Surface Hourly: Asheville, NC, USA, 2001; Available online: https://www.ncdc.noaa.gov/isd/data-access (accessed on 12 April 2018).
40. Justice, C.O.; Townshend, J.R.G.; Vermote, E.F.; Masuoka, E.; Wolfe, R.E.; Saleous, N.; Roy, D.P.; Morisette, J.T. An overview of MODIS land data processing and product status. *Remote. Sens. Environ.* **2002**, *83*, 3–15. [CrossRef]
41. Rienecker, M.M.; Keppenne, C.L.; Kovach, R.; Jacob, J.P.; Marshak, J. The GMAO's Ensemble Kalman Filter Ocean Data Assimilation System. In Proceedings of the Third WCRP International Conference on Reanalysis, Tokyo, Japan, 28 January–1 February 2008.
42. Bosilovich, M.G.; Akella, S.; Coy, L.; Cullather, R.; Draper, C.; Gelaro, R.; Kovach, R.; Liu, Q.; Molod, A.; Norris, P.; et al. *MERRA-2: Initial Evaluation of the Climate, Technical Report Series on Global Modeling and Data Assimilation*; NASA: Washington, DC, USA, 2015.
43. Kim, Y.; Kimball, J.S.; Zhang, K.; McDonald, K.C. Satellite detection of increasing northern hemisphere non-frozen seasons from 1979 to 2008: Implications for regional vegetation growth. *Remote Sens. Environ.* **2012**, *121*, 472–487. [CrossRef]
44. Du, J.; Kimball, J.S.; Azarderakhsh, M.; Dunbar, R.S.; Moghaddam, M.; McDonald, K.C. Classification of Alaska spring thaw characteristics using satellite L-band radar remote sensing. *IEEE Trans. Geosci. Remote Sens.* **2015**, *53*, 542–556.
45. Reichle, R.H.; Liu, Q.; Koster, R.D.; Draper, C.S.; Mahanama, S.P.P.; Partyka, G.S. Land surface precipitation in MERRA-2. *J. Clim.* **2017**, *30*, 1643–1664. [CrossRef]
46. Reichle, R.H.; Draper, C.S.; Liu, Q.; Girotto, M.; Mahanama, S.P.P.; Koster, R.D.; De Lannoy, G.J.M. Assessment of MERRA-2 land surface hydrology estimates. *J. Clim.* **2017**, *30*, 2937–2960. [CrossRef]
47. Draper, C.S.; Reichle, R.H.; Koster, R.D. Assessment of MERRA-2 land surface energy flux estimates. *J. Clim.* **2018**, *31*, 671–691. [CrossRef]
48. Allen, R.G.; Pereira, L.S.; Raes, D.; Smith, M. *Crop Evapotranspiration-Guidelines for Computing Crop Water Requirements-FAO Irrigation and Drainage Paper 56*; FAO: Rome, Italy, 1998.
49. Lawrence, M.G. The relationship between relative humidity and the dewpoint temperature in moist air: A simple conversion and applications. *Bull. Am. Meteorol. Soc.* **2005**, *86*, 225–233. [CrossRef]
50. Monteith, J.; Unsworth, M.H. *Principles of Environmental Physics*, 3rd ed.; Academic Press: London, UK, 2008.
51. Smith, W.L. Note on the relationship between precipitable water and surface dew point. *J. Appl. Meteorol.* **1966**, *5*, 726–727. [CrossRef]
52. Recondo, C.; Pendás, E.; Moreno, S.; Ga de Vicuña, C.; García-Martínez, A.; Abajo, A.; Zapico, E. A simple empirical method for estimating surface water vapour pressure using MODIS near-infrared channels: Applications to northern Spain's Asturias region. *Int. J. Remote Sens.* **2013**, *34*, 3248–3273. [CrossRef]
53. Ashcroft, M.B.; Gollan, J.R. Moisture, thermal inertia, and the spatial distributions of near-surface soil and air temperatures: Understanding factors that promote microrefugia. *Agric. For. Meteorol.* **2013**, *176*, 77–89. [CrossRef]
54. Hughes, L. Climate change and Australia: Trends, projections and impacts. *Austral. Ecol.* **2003**, *28*, 423–443. [CrossRef]
55. Jeffrey, S.J.; Carter, J.O.; Moodie, K.B.; Beswick, A.R. Using spatial interpolation to construct a comprehensive archive of Australian climate data. *Environ. Model. Softw.* **2001**, *16*, 309–330. [CrossRef]
56. Cook, E.R.; Anchukaitis, K.J.; Buckley, B.M.; D'Arrigo, R.D.; Jacoby, G.C.; Wright, W.E. Asian monsoon failure and megadrought during the last millennium. *Science* **2010**, *328*, 486–489. [CrossRef] [PubMed]
57. Lewis, S.L.; Brando, P.M.; Phillips, O.L.; van der Heijden, G.M.; Nepstad, D. The 2010 amazon drought. *Science* **2011**, *331*, 554. [CrossRef] [PubMed]
58. Du, J.; Kimball, J.S.; Shi, J.; Jones, L.A.; Wu, S.; Sun, R.; Yang, H. Inter-calibration of satellite passive microwave land observations from AMSR-E and AMSR2 using overlapping FY3B-MWRI sensor measurements. *Remote Sens.* **2014**, *6*, 8594–8616. [CrossRef]